Proceedings of ALGORITMY 2024
pp. 255–263

AUTOMATIC PATH EXTRACTION INSIDE THE AORTA FROM CT DATA *

KONAN A. ALLALY† AND JOZEF URBÁN‡

Abstract. Segmentation of the aorta is crucial for various medical image analyses, such as the diagnosis of large vessel vasculitis. In this work, we present the extraction of a path inside the aorta from 3D non-contrast CT data using the minimal path approach. We define a suitable potential function to keep the path inside the aorta and as close as possible to the centerline. Using anatomical knowledge, we segment the liver, lungs, and trachea to locate the abdominal aorta, descending aorta, and ascending aorta. Key points are automatically detected by circular Hough Transform using the locations of the liver and trachea. The path inside the aorta is built step by step using the detected key points.

Key words. Vasculitis, minimal path, fast marching, Hough Transform, segmentation, liver, aorta, CT.

AMS subject classifications. 35A18, 58J32, 65D18, 65U07

1. Introduction. Vasculitis is the inflammation of blood vessels of various sizes. The early detection and treatment of vasculitis are crucial to avoid irreversible damage such as loss of vision, kidney failure, and aortic dissection. Various approaches are used to diagnose vasculitis, including biopsy, blood or urine cultures, and imaging [2]. The use of ^{18}F-fluorofeoxyglucose PET/CT (FDG-PET/CT) imaging in the diagnosis and treatment of large vessel vasculitis (LVV) is constantly increasing [1, 2]. LVV mainly affects the aorta and its branches. Image analysis and interpretation are the core of imaging's use in the diagnosis of LVV. The interpretation compares pixel values from a reference region of interest (ROI) defined inside the liver and ROIs defined in the affected aorta regions. The ROIs are detected visually, extracted manually, and used for assessment in clinical routine. We aim to automate the extraction of the ROIs to simplify routine use, increase reproducibility, and improve the results.

This work presents the automatic extraction of a path inside the aorta from CT data using the minimal path approach [3]. The minimal path approach finds the geodesic minimal path between two given points in an image. The extracted path is used for various applications such as path planning [3], detection of optimal trajectory for virtual colonoscopy [21], tubular structure centerline extraction and segmentation [4, 5]. In the context of the diagnosis of LVV, we use the extracted path to define ROIs inside the aorta by defining spherical volumes around each path point. The minimal path approach suffers from the shortcut problem when used for long and curved structures [6], and the extracted path may not be centered. For our application, we define multiple key points to overcome the shortcut problem in the aortic arch. We segment the liver and the carina to detect the abdominal, ascending, and descending aorta by circular Hough Transform (HT). We design a potential function to keep the path inside the aorta and as close as possible to its centerline.

*This project has received funding from the European Union's Horizon 2020 research and innovation programme under the Marie Skłodowska-Curie grant agreement **No. 955576**.

†Department of Mathematics and Descriptive Geometry, Slovak University of Technology in Bratislava (allaly.anderson@stuba.sk) §

‡TatraMed Software s.r.o. (jozef.urban@tatramed.sk)

The paper is organized as follows: section 2 describes the workflow for obtaining a path inside the aorta from 3D non-contrast CT data. In section 3, we present and discuss our results.

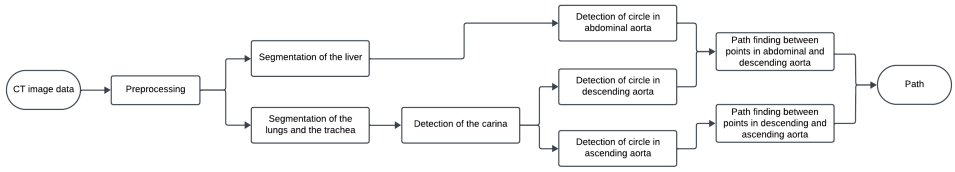

Flow diagram of path extraction inside the aorta

2. Method.

2.1. Data sets and preprocessing. Our data are provided by BIONT, a.s. in Bratislava. The patient data are anonymized by removing personal information to ensure the patient's privacy. The 3D CT image data is made of a sequence of 2D slices. The resolution of the slices is 512×512. The pixel spacing varies from 0.976562 mm to 1.171875 mm, and the spacing between slices varies from 1.5 mm to 2.5 mm. We apply trilinear interpolation to the original image data to have the same spacing in all the directions (x, y, z) to ensure a uniform grid for space discretization. Due to the noise, we applied filtering as preprocessing. We use the Geodesic Mean Curvature Flow (GMCF) for the filtering because it is suitable to remove noise while preserving the edges [9]:

$$u_t = |\nabla u| \ \nabla \cdot \left(g(|\nabla G_\sigma * u|) \frac{\nabla u}{|\nabla u|} \right) \tag{2.1}$$

where u is the input image, $g(s) = \frac{1}{1+Ks^2}$ is an edge detection function and $K > 0$ is a parameter. G_σ is a Gaussian kernel used for smoothing and σ the variance. We use a semi-implicit finite volume scheme for the discretization and a Gauss-Seidel iterative scheme to solve the linear system (see [9] for more details).

2.2. Detection of key points. The minimal path approach requires one or two points to be implemented [3, 6]. We automatically detect key points based on anatomical knowledge to have a path inside the aorta with less user interaction. Each slice containing the liver contains the abdominal aorta as a circular object. The slice containing the carina contains the ascending and the descending aorta [12]. This section presents our approach to segmenting the liver and the carina; then, using the Hough Transform, we detect the key points in the abdominal, ascending, and descending aorta.

2.2.1. Segmentation of the liver. The segmentation of the liver is crucial for various reasons, such as a better understanding of liver anatomy, the diagnosis of liver diseases, or surgical planning. This work uses the segmented liver to locate the abdominal aorta. The segmentation of the liver from CT data is a challenging task due to the proximity of the liver to abdominal organs such as the pancreas, the spleen, or the stomach. The segmentation of the liver has occupied researchers for many years. Various approaches have been used to segment the liver, including thresholding, region growing, active contour, and deep learning models [22, 23, 24]. We performed the segmentation of the liver by a combination of several image processing

techniques, including thresholding, connected components labeling [14], morphological operations, and the Generalized SUBjective SURface (GSUBSURF) method [10, 11]. Our approach is a semi-automatic approach and consists of four steps. We start by applying multilevel thresholding according to the liver pixel value range (−50HU to 199HU) [17]. In the second step, we apply the connected components labeling. The region containing the liver is found to be the largest region. For our data set, the segmented region contains the liver and other organs such as the kidney, the aorta, and some ribs. In the next step, we apply erosion several times to the segmented region to remove the other structures and keep the liver. The erosions shrink the liver, so in the last step, we apply the GSUBSURF model using the segmented volume as the initial condition to refine the segmented liver.

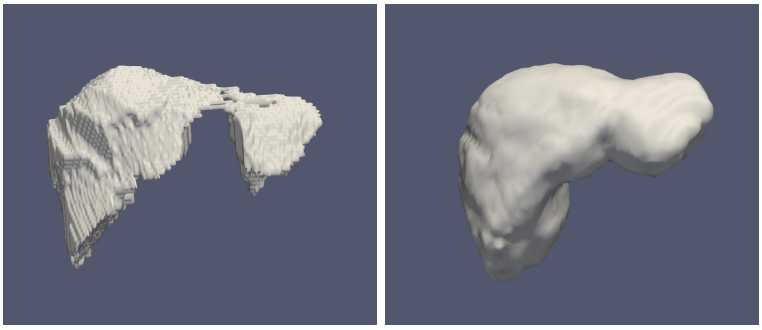

FIG. 2.1. *Liver segmentation from CT data, by thresholding, erosion, connected components labeling and refined by the GSUBSURF method.*

The first image in FIG. 2.1 shows the segmentation of the liver obtained by thresholding, connected components labeling, and seven erosions. The second image shows the refined initial liver segmentation by the GSUBSURF model. We stopped the segmentation at 6000 time steps because the difference (L^2-norm) between the previous and current solutions was small (around 0.001). For visualization, we chose the level set 0.9.

2.2.2. Segmentation of the lungs and the trachea. The trachea is a tube-like structure between the mouth and the parenchyma of the lungs and the carina, which marks its end. The carina is the region where the trachea splits into two segments and is just under the aortic arch [16]. Therefore, detecting or segmenting the trachea can be used to detect the aortic arch, the ascending and descending aorta [12]. The lungs, the trachea, and the carina are all connected, so segmenting the trachea or the carina involves segmenting the lungs. Over the years, various segmentation approaches have been proposed to segment the lungs, see [19] for a detailed review of the literature. We follow a similar approach to authors of [18] to segment the lungs. Our approach to segmenting the lungs consists of three steps. Firstly, we perform thresholding using lung pixels value (−500 HU for our dataset). All the pixels above the threshold are set to 0, and the remaining are set to 1. Connected components labeling is applied to the thresholded data, and the lungs, connected to the trachea, are extracted as the largest region. Next, we apply morphological operations such as erosion and dilatation to disconnect the trachea and the left and right lungs. Finally, the initial segmentation is used as a mask to segment the trachea. The carina is detected as the last slice containing one region before the slice containing two regions.

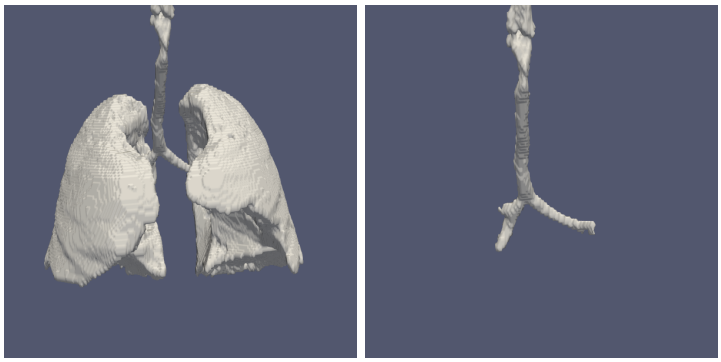

FIG. 2.2. *Lungs and trachea segmented from CT data, by thresholding, erosion, dilatation and connected components labeling.*

2.3. Hough Transform. The HT is used in computer vision to detect shapes such as lines, squares, or circles. The algorithm is mostly applied to edge images. An edge detector such as a Canny edge detector [15] is applied to the input image, and pixels whose value exceeds a defined threshold are kept as edge pixels. If a circle in a 2D image is described as: $(x-a)^2 + (y-b)^2 = r^2$, where (a, b) are coordinates of the center and r the radius, an arbitrary edge point (x_i, y_i) will be transformed into a right circular cone in the (a, b, r) parameters space [20]. For each image point (a, b) and given radius range $[r_{min}, r_{max}]$, an accumulation array is built by voting. The accumulation array for (a, b) and r_i is increased by 1 if an edge point (x_i, y_i) is a solution of the circle equation. At the end of the voting process, the accumulation array contains the number of all the points belonging to the circle. A criterion is then defined based on the accumulation array to decide which point corresponds to a circle center in the image. The original approach is time-consuming and needs a large memory to store the accumulation array. For optimization, our implementation is a local approach (around the carina). We discriminate the edge pixels as non-center. We use the aorta radius range provided in [13] and cumulative ratio (based on voting and given radius) array to find the optimal center. We compute the ratio by dividing the vote of each point by the radius, and the cumulative ratio is the average of the ratios for all the radiuses. We obtain one single circle corresponding to the aorta. This approach allows us, for a given aorta radius range, to detect one circle in the abdominal, the ascending, and the descending aorta.

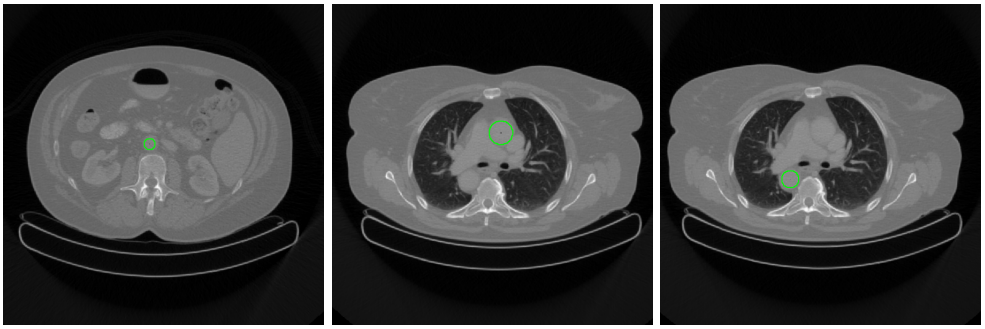

FIG. 2.3. *Abdominal, ascending and descending aorta detected by circular Hough Transform.*

2.4. The minimal path approach. The minimal path approach was introduced in [3] to find the geodesic minimal path between two given points. The minimal path is a curve C connecting two points p_i (starting point), p_f (end point) and minimizes a modified "snake" energy. It detects the global minimum of an active contour model's energy between two endpoints.

2.4.1. Global minimum for active contour. The deformable contour model is a mapping : $C(v) : \Omega \to \mathbb{R}^2$, $v \mapsto (x(v), y(v))$, where $\Omega = [0, 1]$ is the parametrization interval, v is a parameter. We use 2D notations for simplification purposes. The deformable model is a space of admissible paths or deformations $\mathcal{A}$ and a functional E. E represents the energy of the model, which will be minimized on $\mathcal{A}$ and has the following form $E : \mathcal{A} \to \mathbb{R}$:

$$C \mapsto E(C) = \int_\Omega \left(\frac{\omega_1}{2}||C'(v)||^2 + \frac{\omega_2}{2}||C''(v)||^2 + P(C(v)) \right) dv \tag{2.2}$$

where C' and C'' are the first and second derivatives of C with respect to v, and P is the potential function associated to the external forces. The first two terms are internal forces, and the third is image forces. The choice of ω_1 and ω_2 determines the curves' elasticity and rigidity.

2.4.2. Problem formulation. Contrary to the classical snake energy, v is chosen to be the arc-length parameter s, which means $||C'(s)|| = 1$, then $\Omega = [0, L]$, where L is the length of the curve. Therefore, the energy depends only on the geometric curve and not on the parametrization. The second derivative of C is removed from the energy to reduce the user initialization to setting just two endpoints of the curve C. The energy of the new model has the following form: $\mathcal{A}_{p_i,p_f} \to \mathbb{R}$

$$\begin{aligned} C \mapsto E(C(s)) &= \int_0^L \left(\omega||C'(s)||^2 + P(C(s)) \right) ds \\ &= \omega L(C(s)) + \int_0^L P(C(s))\ ds \\ &= \int_0^L (\omega + P(C(s)))\ ds = \int_0^L \tilde{P}(C(s))\ ds \end{aligned}$$

where $\tilde{P}(p) = \omega + P(p)$. $\mathcal{A}_{p_i,p_f}$ is the space of all curves connecting the points p_i and p_f. The boundary conditions are given by $C(0) = p_i$ and $C(L) = p_f$. $\omega > 0$ is used to control the smoothness of the curve.

Given a potential $P > 0$ that takes lower values near desired features, we are looking for paths along which the integral of $\tilde{P}$ is minimal. At each point p of the image, the minimal action U corresponds to the minimal energy integrated along a path that starts at p_i and ends at p:

$$U(p) = \inf_{\mathcal{A}_{p_i,p}} \left(\int_C \tilde{P} ds \right) = \inf_{\mathcal{A}_{p_i,p}} E(C) \tag{2.3}$$

$\mathcal{A}_{p_i,p}$ is the set of all paths between p_i and p.

To compute the minimal action U, the authors of [3] formulated the partial differential evolution equation (related to eq. 2.3):

$$\frac{\partial \mathcal{L}(s,t)}{\partial t} = \frac{1}{\tilde{P}} \vec{n}(s,t) \tag{2.4}$$

to describe the set of equal energy contour $\mathcal{L}$ in time, where t is the value of the energy and $\vec{n}(s,t)$ the normal to the closed curve $\mathcal{L}(.,t)$. The equation (eq. 2.4) evolves a front starting from a small circle around p_0 until U is computed for each point inside the image domain. The authors proposed three approaches to find the minimal action U: *graph search approach*, *shape from shading approach*, and *front propagation approach* [3]. They showed that U satisfies the Eikonal equation:

$$||\nabla U|| = \tilde{P}, \quad U(p_0) = 0. \tag{2.5}$$

In this work, we use the fast marching method [7] to compute U because it is fast and has lower complexity than the other approaches [4].

The gradient of U is orthogonal to the propagating front. Therefore, the minimal path C_{p_i,p_f} between two points p_i and p_f is found by sliding back the minimal action U from p_f until p_i. To find C_{p_i,p_f}, the authors of [4] suggested the steepest descent gradient:

$$p_{n+1} = p_n - \tau \ \times \ \frac{\nabla U}{||\nabla U||}, \quad \tau > 0, \quad n = 0, ..., N \tag{2.6}$$

where p_{n+1} is the next point, p_n the current point and N the maximal number of path points. The iterative process starts with $p_0 = p_f$ and stops when the Euclidian distance between the current point and p_i is less than a defined tolerance ε. The gradient of U is normalized by $||\nabla U||^{-1}$ to have a unit speed of the curve. Some other methods like Runge-Kutta midpoint algorithm or Heun's method can be used to extract the path by solving the following ordinary differential equation [4]:

$$\frac{dC_{p_i,p_f}}{ds}(s) = -\nabla U(C_{p_i,p_f}(s)), \quad C_{p_i,p_f}(0) = p_f \tag{2.7}$$

In this work, we use the descent gradient (eq. 2.6) method to find the minimal path for given points p_i and p_f.

2.4.3. Potential Function. The potential function is based on the image pixel values and pushes the front to the desired regions. The front propagates faster along lower values of the potential function [4]. Defining an appropriate potential function is crucial for obtaining accurate results. Depending on the applications, the authors in [3] suggested some potential functions based on edge detection operators, distance-based potential, and potential using pixel values. Our potential function is defined to extract a path inside the aorta and close to the centerline:

$$\tilde{P}(x) = \omega + \frac{|I_{seed} - I_x|}{max(|I_{seed} - I_x|)} \ \frac{1}{1 + d(x)}, \quad x \in \mathbb{R}^n, \ n = 2, 3. \tag{2.8}$$

I_{seed} is the average of pixels value in spherical volume (3 mm of radius) around the starting point to reduce the noise effect. $\omega > 0$ is a parameter for smoothing the path, and d is the distance map computed on the edge image. The edge image is obtained in two steps. We start by computing the edge detector using the function presented in **section 2.1**. We apply thresholding to the edge detector to have a binary image where the edge pixels value is set to 1 and the other to 0. Then, we compute a signed distance function using the fast sweeping method [8] to the edge image so that

the higher distance for the aorta regions will be located at the center. Therefore, the third term of (eq. 2.8) allows us to have smaller values of the potential function inside the aorta and larger values on the edges. The edges will act as an obstacle to the propagation in the front, allowing faster propagation inside the aorta. The second term is built according to the potential functions suggested in [4]. We normalize the difference by the maximal value to have the term in the interval $[0, 1]$. The second term is enough to obtain a good path for images with high contrast between the region of interest and the other regions. Combining these terms allows us to extract a path in non-contrast CT image data, and the extracted path is close to the centerline for tubular structures such as the aorta.

3. Results and discussion. In this section, we present the extracted paths inside the aorta using the potential function described in **section 2.4.3**. We use the fast marching method [7] to compute the minimal action U and the descent gradient (eq. 2.6) method to find the path C_{p_i,p_f} connecting two given points p_i and p_f, with $\tau = 0.8$ and $\varepsilon = 1$.

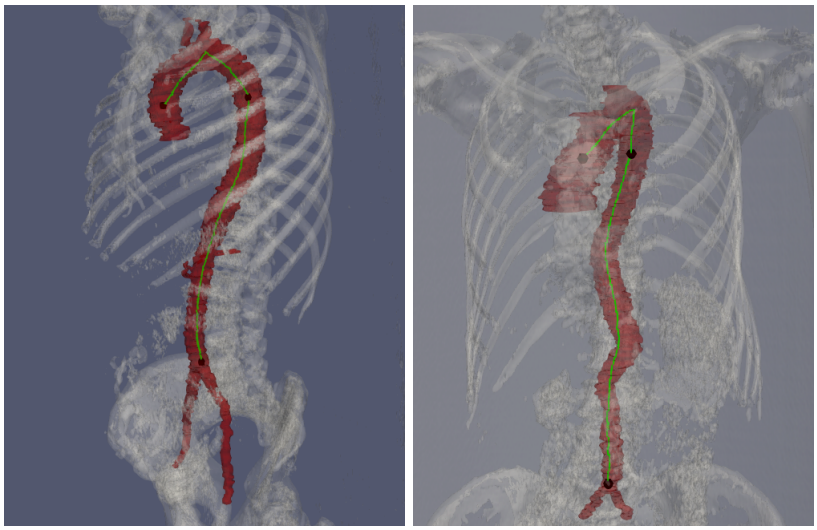

FIG. 3.1. *Extracted paths (green) in 3D image of two different patients.*

The blue dots are the points used for the path extraction. The aorta is segmented manually for visualization purposes. Let's call the points in the abdominal aorta p_1, the descending aorta p_2, and the ascending aorta p_3. Between p_1 and p_2, we perform the minimal path approach to get the first segment of the path. Between p_2 and p_3, we get the path in two steps to avoid the shortcut issue in the aortic arch. First, we use the automatic key points detection approach presented in [6] to find a new point p inside the aorta between p_2 and p_3. In the second step, we find the paths connecting p_2 to p and p to p_3.

The minimal path approach is noise-sensitive, may not lead to a centered path, and suffers from the shortcut issue [5, 6]. The shortcut happens when the structure of interest is long, thin, and curved. We applied the geodesic mean curvature filtering [9] to reduce the noise and its potentially harmful effect. We defined a new potential

function combining pixel values and a distance map to keep the path inside the aorta as close as possible to its centerline. We detected points automatically in the ascending and descending aorta to reduce user interaction and overcome the shortcut issue in the aortic arch. As mentioned in the introduction, the path extraction inside the aorta is part of a framework related to the diagnosis of large vessel vasculitis by FDG-PET/CT imaging. For this purpose, a centered path is better since a good enough estimation of the aorta shape can be obtained using the aorta radius range and the centered path. In future work, we will focus on an efficient implementation of the approach presented in [5] to get a 3D-centered path in a reasonable time. We will also implement the work presented in [21] to obtain another centered path. A comparison of the results for both approaches will be provided. We will also present the diagnosis of patients suspected of having vasculitis using the extracted path.

REFERENCES

[1] L. Arnaud, J. Haroche, Z. Malek, F. Archambaud, L. Gambotti, G. Grimon, A. Kas, N. Costedoat-Chalumeau, P. Cacoub, D. Toledano, P. Cluzel, J. C. Piette and Z. Amoura, *Is 18F-Fluorodeoxyglucose Positron Emission Tomography Scanning a Reliable Way to Asses Disease Activity in Takayasu Arteritis ?*, ARTHRITIS and RHEUMATISM, Volume 60, No. 4, pages 1193-1200, April 2009.

[2] A. Betrains and D. Blockmans, *Diagnostic Approaches for Large Vessels Vasculitides*, Open Acces Rheumatology: Research and Reviews, pages 153-165, (2021).

[3] L. D. Cohen and R. Kimmel, *Global Minimum for Active Contour Models: A Minimal Path Approach*, International Journal of Computer Vision, Volume 24(1), pages 57-78, (1997).

[4] T. Deschamps and L. D. Cohen, *Fast extraction of minimal paths in 3D images and applications to virtual endoscopy*, Medical Image Analysis, Volume 5, pages 281-299, (2001).

[5] H. Li and A. Yezzi, *Vessels as 4-D Curves: Global Minimal 4-D Paths to Extract 3-D Tubular Surfaces and Centerlines*, IEEE TRANSACTIONS ON MEDICAL IMAGING, Volume 26, No. 9, SEPTEMBER 2007.

[6] F. Benmansour and L. D. Cohen, *Fast Object Segmentation by Growing Minimal Paths from a Single Point on 2D or 3D Images*, Journal of Mathematical Imaging and Vision, Volume 33, pages 209-221, (2009).

[7] J. A. Sethian, *A fast marching level set method for monotonically advancing fronts*, In Proceedings of the Natural Academy of Sciences, Volume 93, pages 1591-1595, February 1996.

[8] H. Zhao, *Fast sweeping method for Eikonal equations*, MATHEMATICS OF COMPUTATION, Volume 74, Number 250, pages 603-627, May 2004.

[9] Z. Krivá, K. Mikula, N. Peyriéra, B. Rizzi, A. Sarti and O. Stasová, *3D early embryogenesis image filtering by nonlinear partial differential equations*, Medical Image Analysis, Volume 14, pages 510-526, (2010).

[10] A. Sarti and G. Citti, *Subjective surfaces and Riemannian mean curvature flow of graphs*, In Proceedings of Algoritmy 2000, pages 85-103, (2001).

[11] K. Mikula and M. Remesíková, *Finite volume schemes for the generalized subjective surface equation in image segmentation*, Kybernetika, Volume 45, Number 4, pages 646-656, (2009).

[12] M. Feuerstein, T. Kitasaka and K. Mori, *Automated Anatomical Likelihood Driven Extraction and Branching Detection of Aortic Arch in 3-D Chest CT*, In 2nd International Workshop on Pulmonary Image Analysis, pages 49-60, (2009).

[13] T. Kovács, *Automatic Segmentation of the Vessel Lumen from 3D CTA Images of Aortic Dissection.*, PhD. Thesis, ETH Zurich, 2010.

[14] A. Bovik, *Handbook of image and video processing*, Academic Press, 2000.

[15] J. Canny, *A Computational Approach to Edge Detection*, IEEE TRANSACTIONS ON PATTERN ANALYSIS AND MACHINE INTELLIGENCE, Volume PAMI-8, Number 6, November 1986.

[16] P. W. Furlow and D. J. Mathisen, *Surgical anatomy of the trachea*, Annals of Cardiothoracic Surgery, Volume 7(2), pages 255-260, (2018).

[17] K. Singhrao, C. L. Dugan, C. Calvin, L. Pelayo, S. S. Yom, J. W. -H. Chan, J. E. Scholey, and L. Singer, *Evaluating the Hounsfield unit assignment and dose differences*

between CT-based standard and deep learning-based synthetic CT images for MRI-only radiation therapy of the head and neck, Journal of Applied Clinical Medical Physics, Volume 25, January 2024.

[18] S. Hu, E. A. Hoffman and J. M. Reinhardt, *Automatic Lung Segmentation for Accurate Quantitation of Volumetric X-Ray CT Images*, IEEEE Transactions on medical imaging, Volume 20, No. 6, June 2001.

[19] E. M. van Rikxoort and B. van Ginneken, *Automatic segmentation of the pulmonary structures in thoracic computed tomography scans: a review*, Physics in Medicine and Biology, Volume 58, R187-R220, (2013).

[20] H. K. Yuen, J. Princen, J. Illingworth and J. Kittler, *A comparative Study of Hough Transform Methods for Circle finding*, Image and Vision Computing, Volume 8(1), pages 71-77, February 1990.

[21] K. Mikula and J. Urbán, *A new tangentially stabilized 3D curve evolution algorithm and its application in virtual colonoscopy*, Advances in Computational Mathematics, Volume 40, pages 819-837, (2014).

[22] D. A. B. Oliveira, R. Q. Feitosa, and M. M. Correia, *Segmentation of liver, its vessels and lesions from CT images for surgical planning*, BioMedical Engineering, April 2011.

[23] L. Fernandez-de-Manuel, J. L. Rubio, M. J. Ledesma-Carbayo, J. Pascau, J. M. Tellado, E. Ramon, M. Desco and A. Santos, *3D liver segmentation in preoperative CT images using a level-sets active surface method*, In 31st Annual International conference of the IEEE EMBS, September 2009.

[24] K. E. Sengun, Y. T. Cetin, M. S. Guzel, S. Can and G. E. Bostanci, *Automatic Liver Segmentation from CT Images Using Deep Learning Algorithms: A Comparative Study*, arXiv:2101.09987, January 2021.